

## Article

# Simultaneous Improvement of Strength, Ductility and Damping Capacity of Single $\beta$ -Phase Mg–Li–Al–Zn Alloys

Xinhe Yang <sup>1,†</sup>, Yang Jin <sup>1,†</sup>, Ruizhi Wu <sup>1,\*</sup>, Jiahao Wang <sup>1,2,\*</sup>, Dan Wang <sup>3</sup>, Xiaochun Ma <sup>1</sup>, Legan Hou <sup>1</sup>, Vladimir Serebryany <sup>4</sup>, Iya I. Tashlykova-Bushkevich <sup>5</sup> and Sergey Ya. Betsofen <sup>6</sup> 

<sup>1</sup> Key Laboratory of Superlight Materials & Surface Technology, Ministry of Education, Harbin Engineering University, Harbin 150001, China

<sup>2</sup> Jiangxi Key Laboratory of Forming and Joining Technology for Aerospace Components, Nanchang Hangkong University, Nanchang 330063, China

<sup>3</sup> Key Laboratory of New Carbon-Based Functional and Super-Hard Materials of Heilongjiang Province, School of Physics and Electronic Engineering, Mudanjiang Normal University, Mudanjiang 157011, China

<sup>4</sup> Baikov Institute of Metallurgy and Materials Science, Russian Academy of Sciences, Moscow 119334, Russia

<sup>5</sup> Physics Department, Belarusian State University of Informatics and Radioelectronics, P.Brovki Str. 6, 220013 Minsk, Belarus

<sup>6</sup> Moscow Aviation Institute (MAI), National Research University, Moscow 125993, Russia

\* Correspondence: rzwu@hrbeu.edu.cn (R.W.); wjhyjyo@163.com (J.W.)

† These authors contributed equally to this work.

**Abstract:** Body-centered cubic (BCC) Mg–Li alloy can be effectively strengthened by with the addition of Al and Zn. However, adding excessive amounts result in reduced mechanical properties and damping capacity of the alloy during subsequent heat treatment and deformation. The effects of solution-hot rolling-aging on the mechanical properties and damping capacity of LAZ1333 alloy and LAZ1366 alloy were studied. The solid solution strengthening greatly increases the hardness of the alloy, but the ductility is extremely poor. The AlLi softening phase precipitated during the subsequent hot rolling and aging process greatly improves the ductility of the alloy, but the excess precipitation of in the AlLi softening phase and the solid solution of excess Zn element are not conducive to the substantial improvement of the strength and ductility of the alloy. Excessive addition of alloying elements is detrimental to the damping capacity of the alloy, but the damping capacity of the alloy can be significantly improved by depleting the number of solute atoms through subsequent ageing treatments. The UTS and FE of as-cast LAZ 1333 alloy are 111 MPa and 16.9%, respectively. The as-aged LAZ1333 alloy has the best mechanical properties and damping capacity, and the UTS and FE are increased by 65.8% and 89.3%, respectively, compared to the as-cast alloy, and the damping capacity increased from 0.011 to 0.015.

**Keywords:** BCC-structured Mg–Li alloy; mechanical properties; damping capacity; aging softening; dislocation strengthening; movable dislocation density



**Citation:** Yang, X.; Jin, Y.; Wu, R.; Wang, J.; Wang, D.; Ma, X.; Hou, L.; Serebryany, V.; Tashlykova-Bushkevich, I.I.; Betsofen, S.Y. Simultaneous Improvement of Strength, Ductility and Damping Capacity of Single  $\beta$ -Phase Mg–Li–Al–Zn Alloys. *Metals* **2023**, *13*, 159. <https://doi.org/10.3390/met13010159>

Academic Editor: Talal Al-Samman

Received: 10 December 2022

Revised: 9 January 2023

Accepted: 10 January 2023

Published: 12 January 2023



**Copyright:** © 2023 by the authors. Licensee MDPI, Basel, Switzerland. This article is an open access article distributed under the terms and conditions of the Creative Commons Attribution (CC BY) license (<https://creativecommons.org/licenses/by/4.0/>).

## 1. Introduction

Mg–Li alloys are widely used in aerospace applications, medical devices, weapons, automobiles and 3C industries due to their low density, high specific stiffness and specific strength, excellent electromagnetic shielding properties and damping properties [1–3]. Based on the Mg–Li binary phase diagram, Mg–Li alloy is completely composed of body-centered cubic (BCC)  $\beta$ -Li single phase when the Li content exceeds 10.3 wt%. Numerous studies have shown that BCC  $\beta$ -Li single phase Mg–Li alloys have excellent ductility but low strength and damping capacity. The disadvantage of low strength and poor damping capacity have limited the further application of Mg–Li alloys to some extent. Generally, the damping capacity and mechanical properties of Mg alloys are an ambivalence, which is confirmed by the available literature [4–6]. At present, the disadvantage of low strength

and poor damping capacity of BCC  $\beta$ -Li single phase Mg–Li alloy can be effectively solved by alloying, heat treatment and plastic deformation. Among them, Al and Zn elements are common alloying elements that can effectively strengthen Mg–Li alloys. The strengthening of the Mg–Li alloy by the Al element is mainly through solid solution strengthening and precipitation strengthening. The generated  $\text{MgLi}_2\text{Al}$  belongs to the strengthening phase, and the transition of metastable phases ( $\text{MgLi}_2\text{Al} \rightarrow \text{AlLi}$ ) is thought to result in age softening, which is decomposed into the AlLi softening phase during the aging process [7]. The Zn element has little damage to the plasticity of the Mg–Li alloy, and it mainly plays the role of solid-solution strengthening in the alloy. Al and Zn elements are added as alloying elements at the same time, which not only gives full play to the advantages of Al and Zn elements, but it also avoids the negative effects of excessive single alloying elements [8–11]. In addition, heat treatments (e.g., solid solution and aging) are effective methods to optimize the microstructure, mechanical properties and damping capacity of Mg–Li alloys. By precipitation of fine second phases to deplete the solute atoms in the matrix, it leads to an increase in dislocation movement distances and thus effectively improves the damping capacity of the alloy. Plastic deformation methods such as rolling can also effectively improve the mechanical properties of Mg–Li alloys through deformation strengthening [12–14]. Liu rolled the Mg–8Li–3Al–2Zn–0.5Y alloy at 200 °C, and found that the grain was elongated, and the tensile strength increased from 200 MPa to 250 MPa with the increase of deformation. Ji rolled the squeezed the Mg–16Li–2.5Zn–2.5Er alloy at room temperature, and observed a large number of dislocations in the alloy. The tensile strength of the alloy increased from 93 MPa as cast to 234 MPa as rolled, and the alloy obtained a high specific strength of 178 kN·m/kg.

In order to prepare Mg–Li matrix alloy with low density and excellent properties, Mg–13Li– $x$ Al– $y$ Zn ( $x = 3, 6$  wt%,  $y = 3, 6$  wt%) alloys was selected as the research object to study the effects of heat treatment and rolling deformation on the mechanical properties and damping capacity of the alloy. Existing studies show that the mechanical properties of the Mg–Li alloy gradually improve with the increase of aluminum content. When the aluminum content is greater than 5–6%, the alloy strength does not improve significantly, but the elongation decreases significantly. Therefore, the aluminum content in Mg–Li–Al alloy is generally lower than 5–6%. When the aluminum content reaches more than 3%, the aluminum will not only dissolve in the alloy matrix, but also appear AlLi phase. Zinc has a high solid solubility (about 6.2%) in magnesium, and with the decrease of temperature, the solid solubility decreases, resulting in aging strengthening. In the process of magnesium lithium alloy alloying, aluminum and zinc are generally added as alloying elements at the same time, so as to give full play to their respective advantages. Therefore, the alloy content for both Zn and Al as 3 and 6 wt%.

## 2. Methods

In this study, Mg–13Li– $x$ Al– $y$ Zn ( $x = 3, 6$  wt%,  $y = 3, 6$  wt%) (LAZ13 $xy$ ) alloys were prepared by melting pure magnesium (99.95 wt%), pure lithium (99.90 wt%), pure aluminum (99.90 wt%) and pure zinc (99.90 wt%) in an induction melting furnace under ambient argon gas. The melt was poured into a steel mold to obtain as-cast specimens. The as-cast alloys were solution treated at 400 °C for 5 h followed by rapid air cooling, and the obtained sample was called the as-solutionized alloy. Subsequently, the solid-solution alloy was rolled at 200 °C at a rolling speed of 600 cm/min. The reduction amount of each pass was 0.2 mm and the total reduction rate was 50% to get the hot-rolled alloy. During the whole rolling process, the roll is not preheated and no lubricant is used. The hot-rolled alloy was then aged at 80 °C for 12 h.

The microstructural observation was performed by optical microscope (OM, LEICA DM-IRM, Leica Microsystems, Wetzlar, Germany), scanning electron microscope (SEM, SU5000, Hitachi High-tech Company, Tokyo, Japan) and transmission electron microscope (TEM, FEI Talos F200X G2, Thermo Fisher Scientific, Waltham, MA, USA). The sample was polished with sandpaper after optical microscope observation, and then corroded with

1% nitrate alcohol for 5 s. After quickly cleaning the sample with alcohol, the surface of the sample was dried. The phase composition of the specimens was measured by X-ray diffraction (XRD, Rigaku TTR-III, Rigaku Corporation, Tokyo, Japan) with Cu-K $\alpha$  radiation at a scanning rate of 5°/min between 20° and 80°. The tensile fracture morphologies of the specimens were observed by scanning electron microscope (SEM, JSM-6480A, JEOL, Tokyo, Japan).

The hardness of LAZ13 $xy$  ( $x = 3, 6$  wt%,  $y = 3, 6$  wt%) alloys was measured by Vickers hardness testing with a load of 200 gf and a duration of 15 s. For each specimen, at least eight indents were performed, and the average values were used. The strength and elongation of these alloys were measured with tensile tester (1 mm/min of the tensile rate). The average values were obtained from three parallel tensile tests. The damping capacity was measured by a dynamic mechanical analyzer in single-cantilever vibration mode (TA-DMA Q800, New Castle, DE, USA), and the vibration frequency is 1 Hz. The dimensions of the specimen are 35 mm  $\times$  10 mm  $\times$  1 mm.

### 3. Result and Discussion

#### 3.1. Microstructures and Hardness

Figure 1 manifests the microstructures of as-cast LAZ13 $xy$  ( $x = 3, 6$  wt%,  $y = 3, 6$  wt%) alloys. The grain size of the as-cast LAZ1333 alloy are coarse, with an average size of 223  $\mu$ m. In addition, a small amount of second-phase particles precipitated inside the grains and at the grain boundaries. Compared with the as-cast LAZ1333 alloy, the as-cast LAZ1366 alloy has smaller grain size, with an average grain size of 153  $\mu$ m, and the amount of second phase precipitated inside the grains and at the grain boundaries is significantly increased. The main reason for the fine grain size of the as-cast LAZ1366 alloy is that the second phase precipitated along the grain boundary during the solidification plays a pinning role, thus hindering the growth of the grains. Figure 2 shows that the as-cast LAZ1366 alloy has more second phases compared to the as-cast LAZ1333 alloy. In order to analyze the second phases, EDS and XRD was carried out on the as-cast LAZ1333 alloy and LAZ1366 alloy. Table 1 shows the EDS results of the second phases marked by the yellow arrows and letters in Figure 2. Combined with the XRD results (Figure 3), we can conclude that the as-cast LAZ1333 alloy and LAZ1366 alloy are composed of  $\beta$ -Li and AlLi phases.

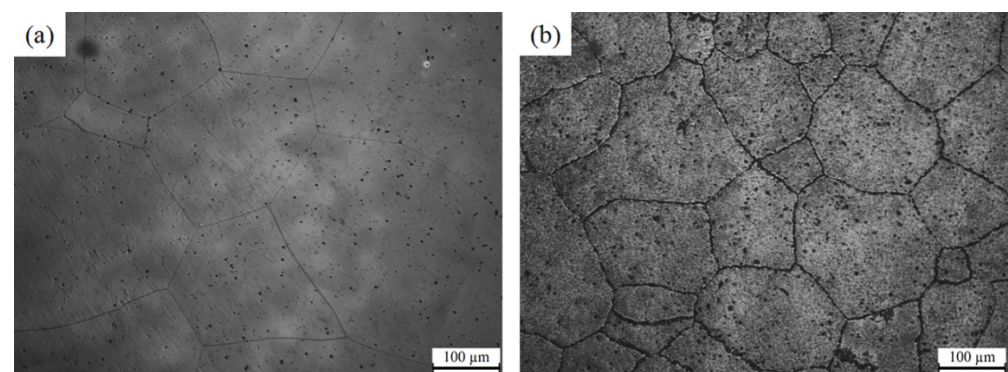


**Figure 1.** The OM images of as-cast LAZ13 $xy$  ( $x = 3, 6$  wt%,  $y = 3, 6$  wt%) alloys: (a) LAZ1333, (b) LAZ1366.

**Table 1.** The EDS results of the second phases marked by the yellow arrows and letters in Figure 2.

Positions	Chemical Compositions (at%)		
	Mg	Al	Zn
A	87.03	9.10	3.87
B	87.20	9.44	3.36
C	90.43	6.79	2.78
D	93.36	4.50	2.14

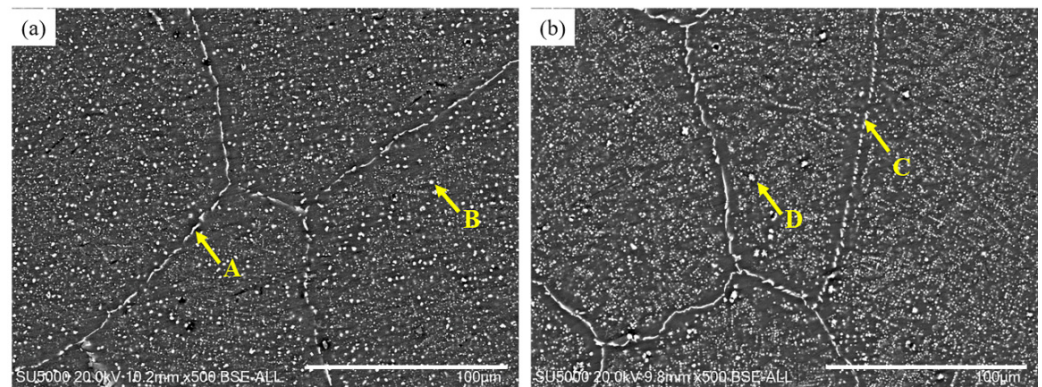


**Figure 2.** The SEM images of as-cast LAZ13 $xy$  ( $x = 3, 6$  wt%,  $y = 3, 6$  wt%) alloys: (a) LAZ1333, (b) LAZ1366.

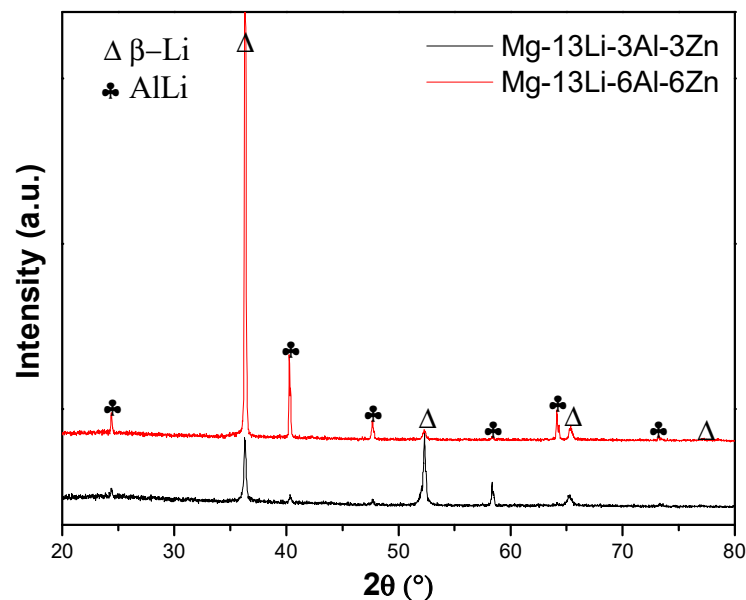


**Figure 3.** The XRD patterns of as-cast LAZ13 $xy$  ( $x = 3, 6$  wt%,  $y = 3, 6$  wt%) alloys.

The as-cast LAZ1366 alloy was then subjected to TEM analysis. As shown in Figure 4a, the precipitation phase in the alloy is micrometer-scale, and the spinodal decomposition appears around the precipitation phase. The HRTEM characterization of the spinodal decomposition is shown in Figure 4b. Figure 4c is the FFT result of region 1, which shows a typical BCC[001] axis, which is  $\beta$ -Li matrix. Figure 4d shows the FFT result of the spinodal decomposition in region 2, which shows a typical BCC[ $\bar{1}22$ ] axis. According to the HAADF-STEM and EDS results shown in Figure 5, these micrometer-scale precipitates hardly contain Mg elements, and only contain Al and Zn elements. It can be seen from the EDS results that the atomic ratio of Al and Zn elements in the precipitation phase is close to 3:1. Combining with the XRD results (Figure 3) and related literature [15–17], the micrometer-scale precipitation phase is AlLi phase. However, no Zn-containing compounds were found in LAZ1333 alloy and LAZ1366 alloy, which was mainly because the maximum solid solubility of Zn in Mg is about 6.2 wt.%, and the Zn element was completely dissolved in the matrix [18,19].

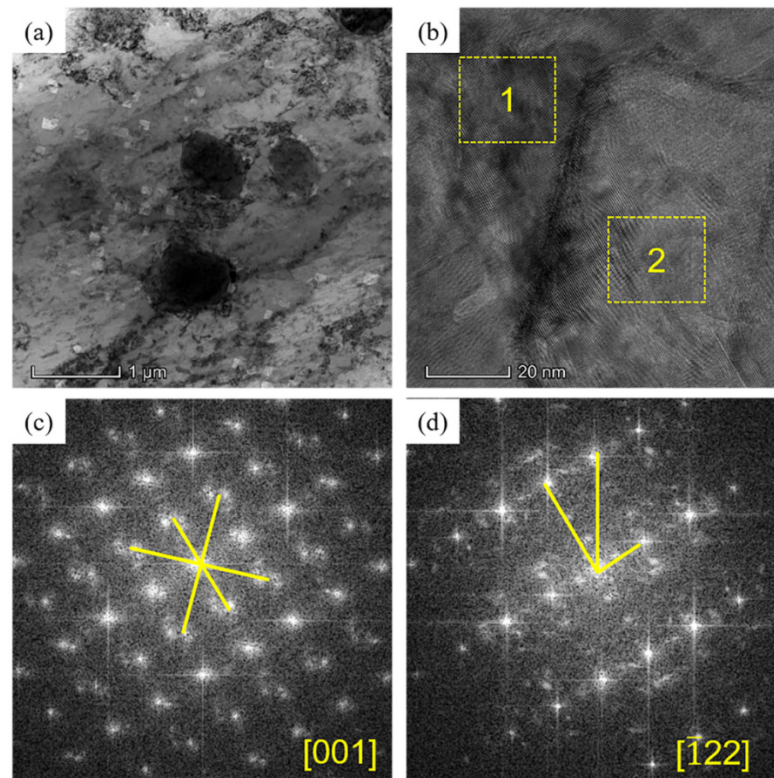


**Figure 4.** (a) TEM image and (b) HRTEM image of spinodal decomposition organization in the as-cast LAZ1366 alloy; FFT results of (c) area 1 and (d) area 2 in (b).

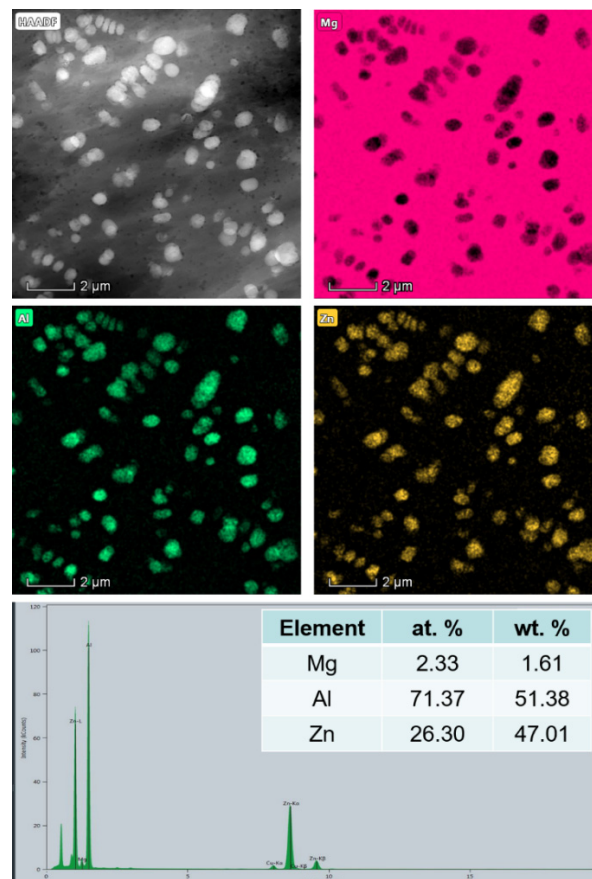


**Figure 5.** HADDF-STEM image of as-cast LAZ1366 alloy and its elemental mapping.

The as-cast alloy was subjected to solution treatment at 400 °C for 5 h. Figure 6a,b show the microstructures of the as-solutionized LAZ13 $xy$  ( $x = 3, 6$  wt%,  $y = 3, 6$  wt%) alloys. It can be seen that the second phase inside the grains and at the grain boundaries in the as-cast alloy disappears, and the average grain sizes of the alloys are 187  $\mu\text{m}$  and 180  $\mu\text{m}$ , respectively. Then the XRD analysis of the as-solutionized alloy was carried out. From Figure 6c, both the as-solutionized LAZ1333 alloy and the as-solutionized LAZ1366 alloy only have the diffraction peaks of the  $\beta$ -Li phase, which indicates that the AlLi phase is completely dissolved into the matrix. As shown in Figure 7, the hardness of as-cast LAZ1333 alloy and LAZ1366 alloy are 45.2 Hv and 57 Hv, respectively. After solution treatment, the hardness values are increased to 110.6 Hv and 121.3 Hv, respectively. The significant increase in the hardness of the as-solutionized alloys is caused by the decomposition of the AlLi softening phase and the solid solution of Al and Zn elements. The heat flux stress of alloy can be calculated by Al content. The higher the Al content, the higher the heat flux stress, and the higher the creep resistance may be. Therefore, the hardness of as-cast and solid-solution LAZ1366 alloy is higher [20].

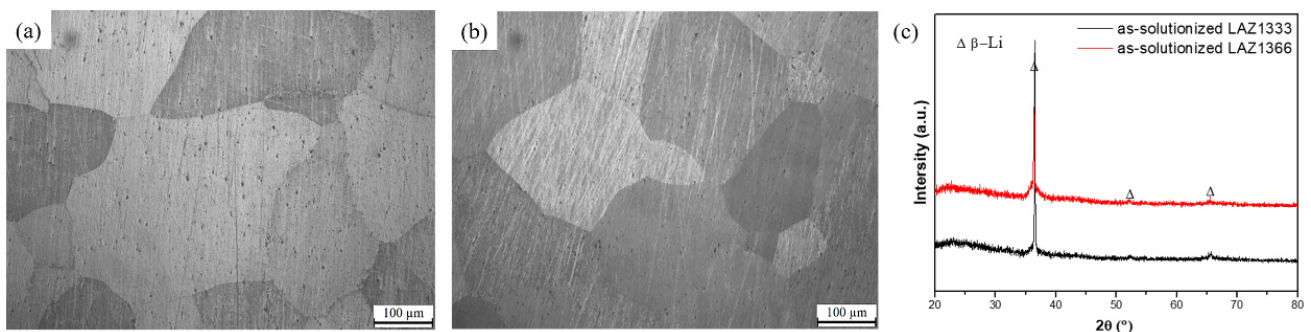


**Figure 6.** The microstructure of as-solutionized LAZ13 $xy$  ( $x = 3, 6$  wt%,  $y = 3, 6$  wt%) alloys: OM images of (a) LAZ1333 and (b) LAZ1366, (c) XRD pattern.

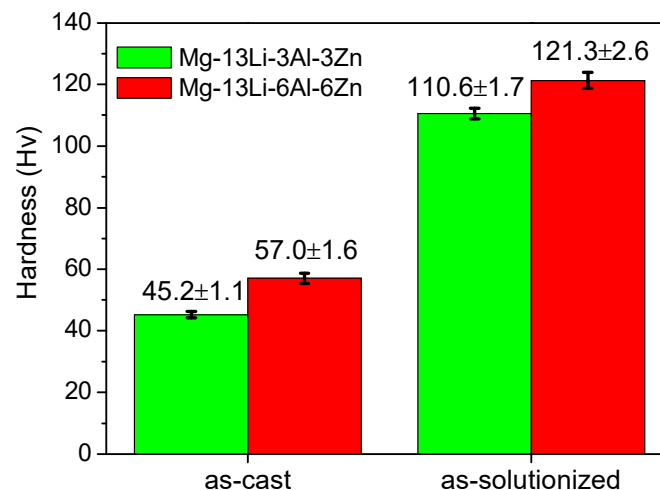


**Figure 7.** Hardness histograms for as-cast and as-solutionized LAZ13 $xy$  ( $x = 3, 6$  wt%,  $y = 3, 6$  wt%) alloys.

The as-solutionized alloy was hot rolled at 200 °C, and the phase analysis of the alloy is shown in Figure 8a. The hot rolling resulted in dynamic precipitation of the AlLi phase. In general, the dynamic precipitation depends on the diffusion rate of atoms during thermal deformation [21]. Plastic deformation leads to a large number of dislocations and vacancies, which can provide additional channels for atomic diffusion [22]. Secondly, the solid solution treatment was carried out at 400 °C, but the rolling temperature was 200 °C. The decrease in temperature leads to a decrease in the solubility of the Al and Zn atoms,

which stimulates the precipitation of solute atoms from the supersaturated matrix in the form of a second phase [23–25]. It can be seen from Figure 8b that the hardness values of the hot-rolled LAZ1333 alloy and hot-rolled LAZ1366 alloy are reduced to 85.3 Hv and 71 Hv, respectively. It is worth noting that the hardness of hot-rolled LAZ1366 alloy greatly decreases, which is mainly caused by the excessive precipitation of the AlLi phase. As shown in Figure 8b, the hardness of LAZ1333 alloy reached the lowest point at 1 h of aging, and then gradually increases, reaching equilibrium after 4 h with a value of 74 Hv. The hardness of LAZ1366 alloy gradually decreases with the increase of aging time, and the hardness is 65.4 Hv when aging for 4 h. Figure 9a,b show the SEM images of the as-aged (80 °C—4 h) LAZ13xy ( $x = 3, 6 \text{ wt\%}$ ,  $y = 3, 6 \text{ wt\%}$ ) alloy. It can be seen that many granular second phases are precipitated in the LAZ1333 and LAZ1366 alloys, and there are more granular second phases and larger sizes in the LAZ1366 alloy. Table 2 shows the EDS results of the second phases marked by the yellow arrows and letters in Figure 9 a,b. From the XRD pattern results in Figure 9c, it can be seen that the as-aged LAZ1333 alloy and LAZ1366 alloy only have the diffraction peaks of the  $\beta$ -Li phase and AlLi phase. The decrease in the hardness of the as-aged alloy is caused by the precipitation of the AlLi phase consuming the Al atoms in the matrix.

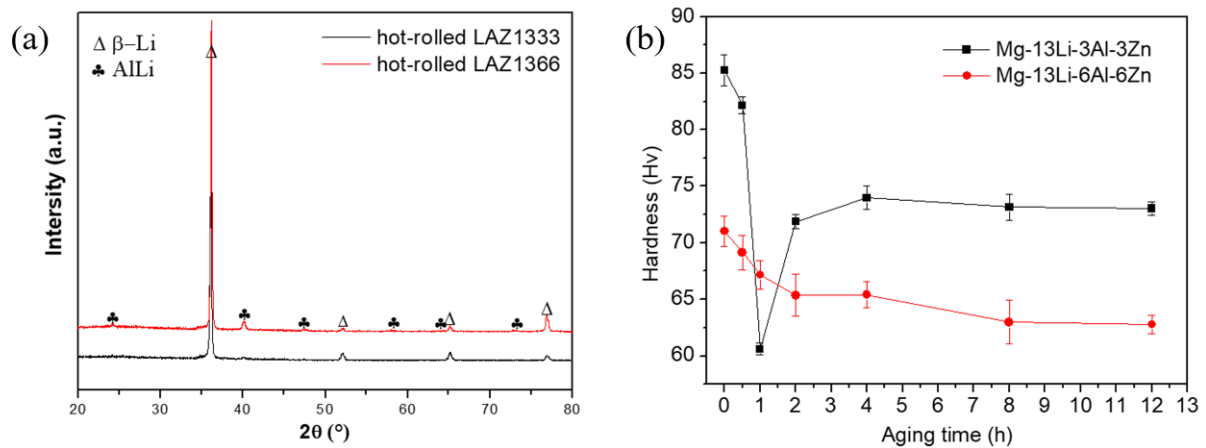


**Figure 8.** (a) XRD pattern of hot-rolled LAZ13xy ( $x = 3, 6 \text{ wt\%}$ ,  $y = 3, 6 \text{ wt\%}$ ) alloys, (b) aging hardening curves of the LAZ13xy ( $x = 3, 6 \text{ wt\%}$ ,  $y = 3, 6 \text{ wt\%}$ ) alloys at 100 °C.

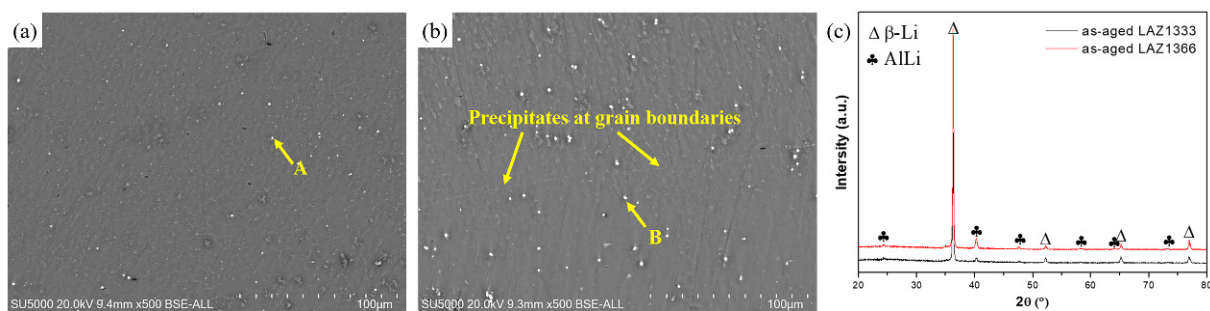


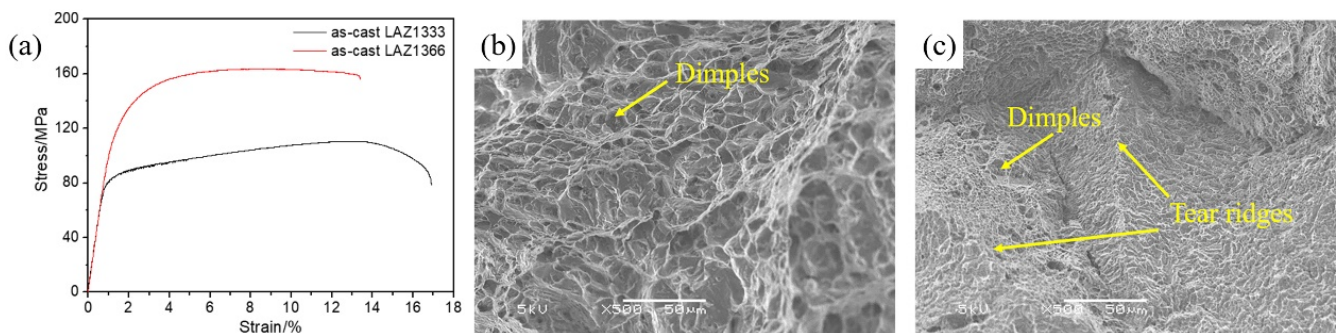
**Figure 9.** The microstructure of as-aged LAZ13xy ( $x = 3, 6 \text{ wt\%}$ ,  $y = 3, 6 \text{ wt\%}$ ) alloys: SEM images of (a) LAZ1333 and (b) LAZ1366, (c) XRD pattern.

**Table 2.** The EDS results of the second phases marked by the yellow arrows and letters in Figure 9a,b.

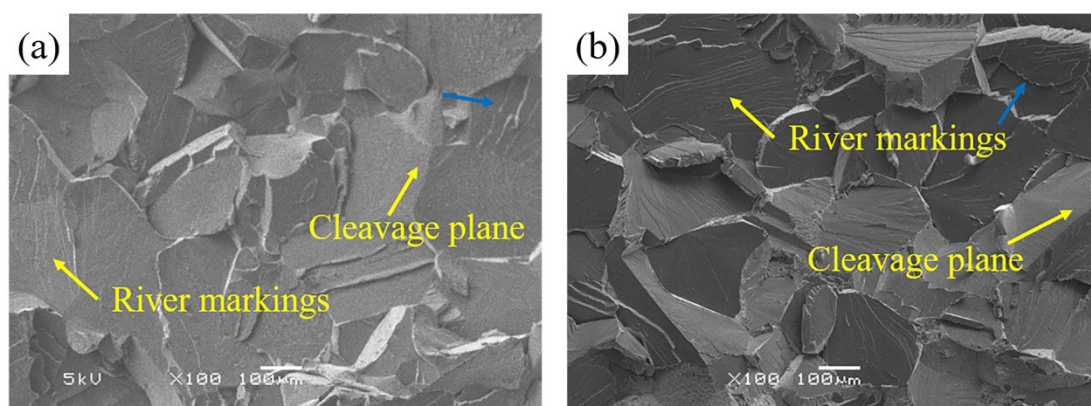
Positions	Chemical Compositions (at%)		
	Mg	Al	Zn
A	72.24	25.94	1.82
B	54.08	43.95	1.97

### 3.2. Mechanical Properties

Figure 10 shows the tensile stress–strain curves for as-cast LAZ1333 and LAZ1366, coupled with SEM fracture morphology. The ultimate tensile strength (UTS) of the as-cast LAZ1333 and LAZ1366 are only 111 MPa and 164 MPa, while the fracture elongations (FE) are 16.9% and 13.4%. The presence of excessive Al and Zn elements in the matrix gives LAZ1366 alloys higher strength. The overall fracture characterization of as-cast LAZ1333 alloy exhibits typical ductile fracture with many large and deep dimples. The fracture surface of as-cast LAZ1366 alloy is composed of tearing ridges and small amounts of dimples, indicating a mixed fracture of brittle and ductile. Figure 1b shows that there are too many precipitates precipitated along grain boundaries in LAZ1366 alloy, which greatly hinders the dislocations initiating and slipping within these zones. Therefore, the FE of as-cast LAZ1366 alloy is lower than that of as-cast LAZ1333 alloy. However, a complete tensile curve cannot be obtained due to the extremely poor plasticity of the as-solutionized alloy. From the SEM fracture morphology of Figure 10, it can be seen that the overall fracture characteristics of the as-solutionized alloy show intergranular fracture with some cleavage fractures. Some cleavage facets contain a number of shallow river markings. Typically, the river markings were expanded to the entire grain from a small zone and are parallel to each other. However, some of the river markings are radial or irregular (blue arrow grain in Figure 11), which could be ascribed to the cracking originated from local grain boundary decohesion [21].



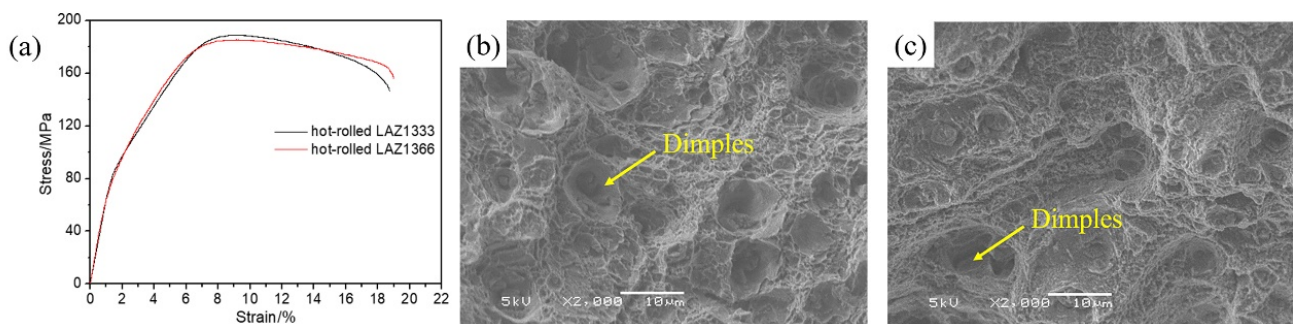
**Figure 10.** Room temperature tensile stress–strain curves and fracture morphology of the as-cast LAZ13 $xy$  ( $x = 3, 6$  wt%,  $y = 3, 6$  wt%) alloys: (a) tensile stress–strain curves, fracture morphology of as-cast (b) LAZ1333 and (c) LAZ1366.



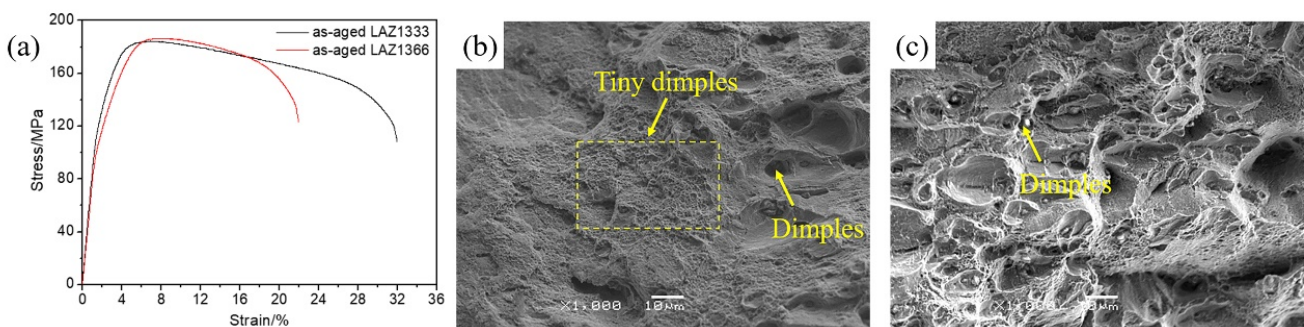
**Figure 11.** Tensile fracture morphology of the as-solutionized LAZ13 $xy$  ( $x = 3, 6$  wt%,  $y = 3, 6$  wt%) alloys: (a) LAZ1333, (b) LAZ1366.

Figure 12 shows the tensile stress–strain curves for as-rolled LAZ1333 and LAZ1366, coupled with SEM fracture morphology. The UTS of as-rolled LAZ1333 alloy and LAZ1366 alloy are 189 MPa and 186 MPa, and the FE are 18.7% and 19%, respectively. The fractures

of the as-rolled LAZ1333 alloy and LAZ1366 alloy are mainly composed of large and deep dimples, showing an obvious ductile fracture characteristic. The improvement of UTS of the as-rolled alloy is mainly due to the combined effect of grain refinement strengthening, dislocations strengthening and dispersion strengthening. Compared with the typical brittle fracture of as-solutionized alloys, the transformation of fracture mode of as-rolled alloys is mainly due to the dynamic precipitation of AlLi phase caused by hot rolling, and the precipitated AlLi phase consumes the solid solution at grain boundaries and within grains. The reduction in the content of solute atoms in the matrix reduces the lattice distortion, thus reducing the occurrence of intergranular fracture of the alloy. Figure 13 shows the tensile stress–strain curves for as-aged LAZ1333 and LAZ1366, coupled with SEM fracture morphology. The UTS of the as-aged LAZ1333 alloy and LAZ1366 alloy are 184 MPa and 187 MPa, which are 65.8% and 14% higher than those of the as-cast alloy. It is worth noting that the FE of the as-aged LAZ1333 alloy is significantly improved, and its value is 32%. From the SEM fracture morphology, the as-aged LAZ1333 alloy contains many small dimples in addition to large and deep dimples compared with the as-aged LAZ1366 alloy.



**Figure 12.** Room temperature tensile stress–strain curves and fracture morphology of the hot-rolled LAZ13 $xy$  ( $x = 3, 6$  wt%,  $y = 3, 6$  wt%) alloys: (a) tensile stress–strain curves, fracture morphology of hot-rolled (b) LAZ1333 and (c) LAZ1366.



**Figure 13.** Room temperature tensile stress–strain curves and fracture morphology of the as-aged LAZ13 $xy$  ( $x = 3, 6$  wt%,  $y = 3, 6$  wt%) alloys: (a) tensile stress–strain curves, fracture morphology of as-aged (b) LAZ1333 and (c) LAZ1366.

The UTS and FE of LAZ13 $xy$  ( $x = 3, 6$  wt%,  $y = 3, 6$  wt%) alloys in the different states are shown in Figure 14. In general, the as-aged LAZ1333 alloy has the best mechanical properties, with its UTS increased by 65.8% and its FE increased by 89.3% compared with the as-cast LAZ1333 alloy. The reason why the UTS and FE of the as-aged LAZ1366 alloy cannot be greatly improved is mainly due to the excess precipitation of the AlLi softening phase and the solid solution of excess Zn element.

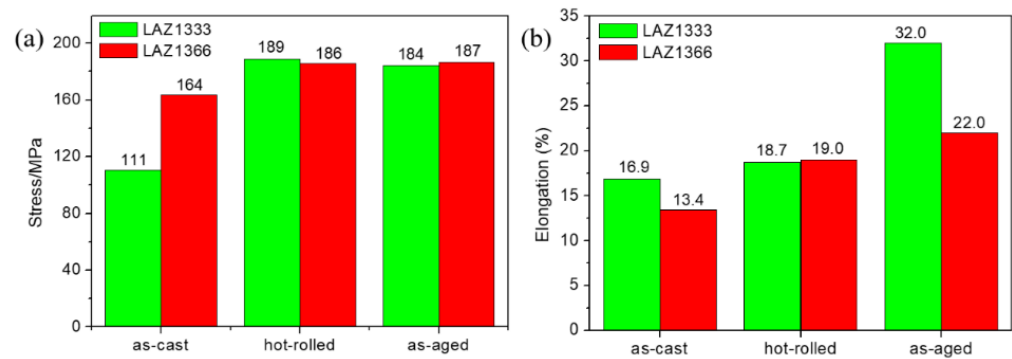


**Figure 14.** Histograms of mechanical properties of the LAZ13 $xy$  ( $x = 3, 6$  wt%,  $y = 3, 6$  wt%) alloys in different states: (a) ultimate tensile strength (UTS), (b) fracture elongation (FE).

### 3.3. Damping Properties

Figure 15 shows damping values  $Q^{-1}$  of the LAZ13 $xy$  ( $x = 3, 6$  wt%,  $y = 3, 6$  wt%) alloys in different states as a function of strain amplitude  $\varepsilon$ . All curves can be divided into two parts. Under the low-strain amplitude stage (region 1),  $Q^{-1}$  is insensitive and grows slowly with  $\varepsilon$ , which is referred to as the strain-amplitude-independent damping. When the strain amplitude exceeds a critical value  $\varepsilon_{cr}$  (high-strain amplitude stage), the  $Q^{-1}$  substantially increases with  $\varepsilon$  (region 2), which is referred to as the strain-amplitude-dependent damping [26]. In the as-cast alloy, the LAZ1366 alloy has more solute atoms compared to LAZ1333 alloy. It is well known that the dislocations are weakly pinned by solute atoms and other point defects during the low-strain amplitude stage (region 1), and the dislocation motion between the weak pinning points generates energy dissipation. The longer the distance between the weak pinning points, the more energy is dissipated by the dislocation motion and the higher the damping capacity of the alloy [27]. The greater number of solute atoms shortens the distance of dislocation movement, which is detrimental to the damping capacity of the alloy [28,29]. Therefore, the damping capacity of as-cast LAZ1366 alloy is lower in the low-strain amplitude stage compared to as-cast LAZ1333 alloy. After heat treatments and plastic deformations, the damping capacity of the as-aged alloys are further improved, and their damping value  $Q^{-1}$  in the low-strain amplitude stage is larger than 0.014, which is approximately twice that of the as-cast alloys. Compared with the as-cast alloys, a finely dispersed AlLi phase is present in the as-aged alloys. The precipitation of the second phase consumes the solute atoms in the matrix, and the decrease in the number of solute atoms leads to an increase in the distance of dislocation movement, thereby improves the damping capacity of the alloy in the low-strain amplitude region. In the high-strain amplitude stage (region 2), the dislocations are still bound by the strong pinning point such as precipitates, grain boundaries, twin boundaries, stacking faults, etc. The damping value  $Q^{-1}$  of the alloy in different states display a sharply increasing trend with an increase of strain amplitude  $\varepsilon$ . Totally, the damping value  $Q^{-1}$  in the high-strain amplitude stage of the as-aged alloys are obviously higher than that of the as-cast alloys. After ageing treatment, the primary phases in the as-cast alloy undergo dissolution and reprecipitation and the distances between AlLi phases increase slightly, thus increases the range of dislocation motion in the matrix. Therefore, the as-aged alloys have the best damping capacity.

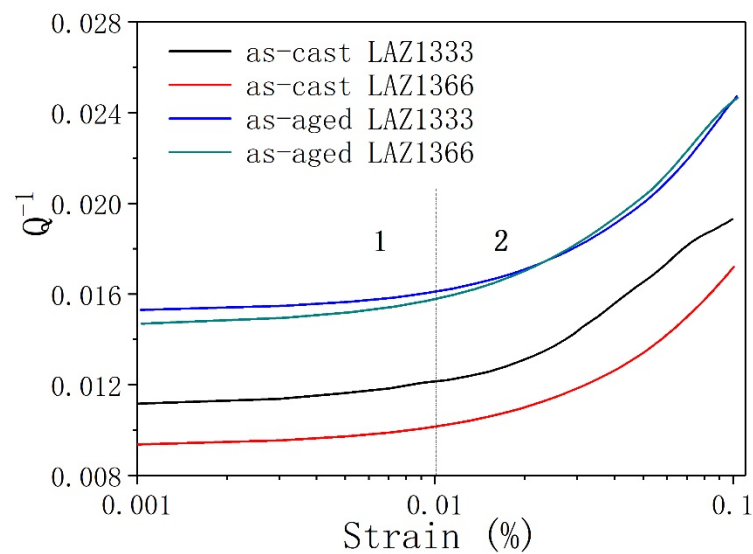


**Figure 15.** Dependence of the damping capacity of the LAZ13xy ( $x = 3, 6$  wt%,  $y = 3, 6$  wt%) alloys in different states as a function of strain amplitude tested.

#### 4. Conclusions

- (1) Both as-cast LAZ1333 alloy and LAZ1366 alloy are composed of  $\beta$ -Li phase and AlLi phase. After the solid solution treatment, the AlLi phase is dissolved, but the hot rolling and subsequent aging make the AlLi phase re-precipitate and disperse in the matrix;
- (2) The as-aged LAZ1333 alloy has the best mechanical properties, and its UTS and FE are 184 MPa and 32%, respectively. The UTS and FE of as-aged LAZ1333 alloy increased by 65.8% and 89.3% higher than that of the as-cast alloy. It can be mainly attributed to the combined effect of grain refinement strengthening, dislocations strengthening and dispersion strengthening;
- (3) The reason why the UTS and FE of the as-aged LAZ1366 alloy cannot be greatly improved is mainly due to the excess precipitation of AlLi softening phase and the solid solution of excess Zn element;
- (4) The as-aged state of LAZ1333 and LAZ1366 alloys exhibits higher damping capacity than as-cast state, and their damping value in the low-strain amplitude stage is larger than 0.014. The improvement in damping capacity is mainly attributed to the increase in the distance of dislocation movement due to the decrease in the number of solute atoms in the matrix.

**Author Contributions:** Validation, L.H. and S.Y.B.; formal analysis, X.Y. and Y.J.; investigation, X.Y., D.W. and V.S.; data curation, J.W.; writing—original draft preparation, X.Y.; writing—review and editing, X.M. and I.I.T.-B.; supervision, R.W. All authors have read and agreed to the published version of the manuscript.

**Funding:** This paper was supported by National Natural Science Foundation of China (51871068, 51971071, 52011530025, U21A2049, 52271098), Fundamental Research Funds for the Central Universities (3072022QBZ1002).

**Data Availability Statement:** The data presented in this study are available in this article.

**Conflicts of Interest:** The authors declare no conflict of interest.

## References

1. Wang, J.; Du, C.; Wu, R.; Xu, L.; Feng, J.; Zhang, J.; Hou, L.; Liu, M.; Liu, B. Effect of Li content on electromagnetic shielding effectiveness in binary Mg–Li alloys: A combined experimental and first-principles study. *J. Mater. Sci. Mater. Electron.* **2022**, *33*, 3891–3900. [[CrossRef](#)]
2. Wang, J.; Xu, L.; Wu, R.; Feng, J.; Zhang, J.; Hou, L.; Zhang, M. Enhanced electromagnetic interference shielding in a duplex-phase Mg–9Li–3Al–1Zn alloy processed by accumulative roll bonding. *Acta Metall. Sin. (Engl. Lett.)* **2020**, *33*, 490–499. [[CrossRef](#)]
3. Hou, P.; Li, F.; Wu, R.; Gao, R.; Zhang, A. Annealing coordinates the deformation of shear band to improve the microstructure difference and simultaneously promote the strength-plasticity of composite plate. *Mater. Des.* **2022**, *219*, 110696.
4. Ren, L.; Quan, G.; Xu, Y.; Yin, D.; Lu, J.; Dang, J. Effect of heat treatment and predeformation on damping capacity of cast Mg–Y binary alloys. *J. Alloys Compd.* **2017**, *699*, 976–982. [[CrossRef](#)]
5. Ma, X.; Jin, S.; Wu, R.; Wang, J.; Wang, G.; Krit, B.; Betsofen, S. Corrosion behavior of Mg–Li alloys: A review. *Trans. Nonferrous Met. Soc. China* **2021**, *31*, 3228–3254. [[CrossRef](#)]
6. Yan, H.; Zhou, X.; Gao, X.; Chen, J.; Xia, W.; Su, B.; Song, M. Development of the finegrained Mg–0.6Zr sheets with enhanced damping capacity by high strain rate rolling. *Mater. Charact.* **2021**, *172*, 110826. [[CrossRef](#)]
7. Wang, J.; Sun, D.; Wu, R.; Du, C.; Yang, Z.; Zhang, J.; Hou, L. A good balance between mechanical properties and electromagnetic shielding effectiveness in Mg–9Li–3Al–1Zn alloy. *Mater. Charact.* **2022**, *188*, 111888. [[CrossRef](#)]
8. Dobkowska, A.; Adamczyk, B.; Kuc, D.; Hadasik, E.; Płociński, T.; Bińczyk, E.; Mizera, J. Influence of bimodal grain size distribution on the corrosion resistance of Mg–4Li–3Al–1Zn (LAZ431). *J. Mater. Res. Technol.* **2021**, *13*, 346–358. [[CrossRef](#)]
9. Dobkowska, A.; Adamczyk, B.; Towarek, A.; Maj, P.; Bińczyk, E.; Momeni, M.; Kuc, D.; Hadasik, E.; Mizera, J. The influence of microstructure on corrosion resistance of Mg–3Al–1Zn–15Li (LAZ1531) alloy. *J. Mater. Eng. Perform.* **2020**, *29*, 2679–2686. [[CrossRef](#)]
10. Ji, H.; Peng, X.; Zhang, X.; Liu, W.; Wu, G.; Zhang, L.; Ding, W. Balance of mechanical properties of Mg–8Li–3Al–2Zn–0.5Y alloy by solution and low-temperature aging treatment. *J. Alloys Compd.* **2019**, *791*, 655–664. [[CrossRef](#)]
11. Sun, Y.; Wang, R.; Peng, C.; Wang, X. Microstructure and corrosion behavior of as-homogenized Mg–xLi–3Al–2Zn–0.2Zr alloys (x = 5, 8, 11 wt%). *Mater. Charact.* **2020**, *159*, 110031. [[CrossRef](#)]
12. Peng, X.; Liu, W.; Wu, G.; Ji, H.; Ding, W. Plastic deformation and heat treatment of Mg–Li alloys: A review. *J. Mater. Sci. Technol.* **2022**, *99*, 193–206. [[CrossRef](#)]
13. Ji, Q.; Wang, Y.; Wu, R.; Wei, Z.; Ma, X.; Zhang, J.; Hou, L.; Zhang, M. High specific strength Mg–Li–Zn–Er alloy processed by multi deformation processes. *Mater. Charact.* **2020**, *160*, 110135. [[CrossRef](#)]
14. Sun, Y.; Wang, R.; Ren, J.; Peng, C.; Feng, Y. Hot deformation behavior of Mg–8Li–3Al–2Zn–0.2Zr alloy based on constitutive analysis, dynamic recrystallization kinetics, and processing map. *Mech. Mater.* **2019**, *131*, 158–168. [[CrossRef](#)]
15. Liang, X.; Peng, X.; Ji, H.; Liu, W.; Wu, G.; Ding, W. Microstructure and mechanical properties of as-cast and solid solution treated Mg–8Li–xAl–yZn alloys. *Trans. Nonferrous Met. Soc. China* **2021**, *31*, 925–938. [[CrossRef](#)]
16. Tang, S.; Xin, T.; Xu, W.; Miskovic, D.; Sha, G.; Quadir, Z.; Ringer, S.; Nomoto, K.; Birbilis, N.; Ferry, M. Precipitation strengthening in an ultralight magnesium alloy. *Nat. Commun.* **2019**, *10*, 1003. [[CrossRef](#)] [[PubMed](#)]
17. Jin, S.; Ma, X.; Wu, R.; Li, T.; Wang, J.; Krit, B.; Hou, L.; Zhang, J.; Wang, G. Effect of carbonate additive on the microstructure and corrosion resistance of plasma electrolytic oxidation coating on Mg–9Li–3Al alloy. *Int. J. Miner. Metall. Mater.* **2022**, *29*, 1453–1463. [[CrossRef](#)]
18. Wang, J.; Wu, R.; Feng, J.; Zhang, J.; Hou, L.; Liu, M. Recent advances of electromagnetic interference shielding Mg matrix materials and their processings: A review. *Trans. Nonferrous Met. Soc. China* **2022**, *32*, 1385–1404. [[CrossRef](#)]
19. Zhang, D.; Shi, G.; Zhao, X.; Qi, F. Microstructure evolution and mechanical properties of Mg–x%Zn–1%Mn (x = 4, 5, 6, 7, 8, 9) wrought magnesium alloys. *Trans. Nonferrous Met. Soc. China* **2011**, *21*, 15–25. [[CrossRef](#)]
20. Mirzadeh, H. A comparative study on the hot flow stress of Mg–Al–Zn magnesium alloys using a simple physically-based approach. *J. Magnes. Alloy* **2014**, *2*, 225–229. [[CrossRef](#)]
21. Wang, J.; Xu, L.; Wu, R.; An, D.; Wei, Z.; Wang, J.; Feng, J.; Zhang, J.; Hou, L.; Liu, M. Simultaneous achievement of high electromagnetic shielding effectiveness (X-band) and strength in Mg–Li–Zn–Gd/MWCNTs composite. *J. Alloys Compd.* **2021**, *882*, 160524. [[CrossRef](#)]
22. Li, W.; Deng, K.; Zhang, X.; Nie, K.; Xu, F. Effect of ultra-slow extrusion speed on the microstructure and mechanical properties of Mg–4Zn–0.5Ca alloy. *Mater. Sci. Eng. A Struct.* **2016**, *677*, 367–375. [[CrossRef](#)]
23. Wang, C.; Kang, J.; Deng, K.; Nie, K.; Liang, W.; Li, W. Microstructure and mechanical properties of Mg–4Zn–xGd (x = 0, 0.5, 1, 2) alloys. *J. Magnes. Alloy* **2020**, *8*, 441–451. [[CrossRef](#)]
24. Liu, W.; Zeng, Z.; Hou, H.; Zhang, J.; Zhu, Y. Dynamic precipitation behavior and mechanical properties of hot-extruded Mg89Y4Zn2Li5 alloys with different extrusion ratio and speed. *Mater. Sci. Eng. A* **2020**, *798*, 140121. [[CrossRef](#)]
25. Tang, S.; Xin, T.; Luo, T.; Ji, F.; Li, C.; Feng, T.; Lan, S. Grain boundary decohesion in body-centered cubic Mg–Li–Al alloys. *J. Alloys Compd.* **2022**, *902*, 163732. [[CrossRef](#)]
26. Wang, J.; Jin, Y.; Wu, R.; Wang, D.; Qian, B.; Zhang, J.; Hou, L. Simultaneous improvement of strength and damping capacities of Mg–8Li–6Y–2Zn alloy by heat treatment and hot rolling. *J. Alloys Compd.* **2022**, *927*, 167027. [[CrossRef](#)]

27. Wang, D.; Liu, S.; Wu, R.; Zhang, S.; Wang, Y.; Wu, H.; Zhang, J.; Hou, L. Synergistically improved damping, elastic modulus and mechanical properties of rolled Mg–8Li–4Y–2Er–2Zn–0.6Zr alloy with twins and long-period stacking ordered phase. *J. Alloys Compd.* **2021**, *881*, 160663. [[CrossRef](#)]
28. Wang, D.; Wu, H.; Wu, R.; Wang, Y.; Zhang, J.; Betsofen, S.; Krit, B.; Hou, L.; Nodir, T. The transformation of LPSO type in Mg–4Y–2Er–2Zn–0.6Zr and its response to the mechanical properties and damping capacities. *J. Magnes. Alloy.* **2020**, *8*, 793–798. [[CrossRef](#)]
29. Qian, B.Y.; Wu, R.Z.; Sun, J.F.; Zhang, J.H.; Hou, L.G.; Ma, X.C.; Wang, J.H.; Hu, H.T. Evolutions of Microstructure and Mechanical Properties in Mg–5Li–1Zn–0.5Ag–0.5Zr–xGd Alloy. *Acta Metall. Sin. (Engl. Lett.)* **2023**. [[CrossRef](#)]

**Disclaimer/Publisher’s Note:** The statements, opinions and data contained in all publications are solely those of the individual author(s) and contributor(s) and not of MDPI and/or the editor(s). MDPI and/or the editor(s) disclaim responsibility for any injury to people or property resulting from any ideas, methods, instructions or products referred to in the content.